the other hand, the basic $4a_0 \times 4a_0$ checkerboard state with its $4/3a_0 \times 4/3a_0$ modulations and pseudogap variations changes subtly so that the $A(\mathbf{R}, E)$ (insets in Fig. 4) appear very similar between dopings. Thus, the checkerboard electronic state appears for $x \leq 0.08$ in the ZTPG regime but continues to exist for $p > p_{SC}$, the critical doping for superconductivity.

We recently introduced a conjecture on underdoped Bi-2212 electronic structure[4,14] which can help to clarify these observations. In **k**-space we distinguish two regions. The first consists of low-energy states on the Fermi arc surrounding the gap nodes. They support a nodal metal at $p < p_{SC}$[9], which becomes a superconductor at $p > p_{SC}$. Second, the high-energy states near the first Brillouin zone-face are incoherent at low doping owing to localization in an electronic crystal state[4]. At low dopings, these high-energy electronic crystal states are unperturbed by the conversion of low-energy states from a nodal metal to a superconductor. This conjecture predicts that the Na-CCOC checkerboard state would be unperturbed by the transition to superconductivity for dopings near $p_{SC}$, consistent with observations.

Angle-resolved photoemission spectroscopy (ARPES) studies of Na-CCOC do indeed detect two very different **k**-space regions, a large ($\sim$200 meV) pseudogap around $(\pi, 0)$, plus a coexisting nodal metal or superconductor consisting of states with $|E| < 10$ meV[9] near the nodes—all consistent with our conjecture. In Bi-2212 the near-nodal states at $|E| < 35$ meV are identifiable with superconductivity via quasiparticle interference[4]. But in $x = 0.12$ Na-CCOC, the near-nodal states occur for $|E| < 10$ meV (ref. 9 and Supplementary Fig. 5), a voltage range where we do not yet have enough sensitivity to detect interference patterns (in any material[4]).

The relationship between the checkerboard electronic crystal state in Na-CCOC and the novel electronic phases proposed for copper oxides[14–30] is indeterminate. In the absence of disorder, the orbital-current ordered states[15–17] seem inconsistent with the observations. Although elementary one-dimensional stripes[18–22] also appear inconsistent because of the 90° rotational symmetry of $g(\mathbf{q}, E)$, defect-dominated stripe states[23] or nematic liquid crystal stripes[24] may still be consistent. Checkerboard states due to Fermi surface nesting[14], valence-bond solids[22,25], pair density waves[26,27], hole-pair[22,27,28] or single hole[14,22] Wigner crystals, or the more recently discussed electronic 'supersolids'[29,30], are not inconsistent with data herein. However, none of these proposals captures the intricate spatial and electronic characteristics found in $Ca_{2-x}Na_xCuO_2Cl_2$. Detailed theory of atomic-scale spectroscopic signatures for the various phases will be required to discriminate between them.

Independently of its microscopic identity, the Na-CCOC checkerboard state is significant because it exemplifies a (no longer hidden) electronic order associated with the copper-oxide pseudogap, and this order is not a translationally invariant liquid of electronic excitations but rather some form of electronic crystal. □

Received 24 February; accepted 13 July 2004; doi:10.1038/nature02861.


1. Timusk, T. & Statt, B. The pseudogap in high-temperature superconductors: an experimental survey. *Rep. Prog. Phys.* **62,** 61–122 (1999).
2. Hoffman, J. E. *et al.* A four unit cell periodic pattern of quasi-particle states surrounding vortex cores in $Bi_2Sr_2CaCu_2O_{8+\delta}$. *Science* **295,** 466–469 (2002).
3. Vershinin, M. *et al.* Local ordering in the pseudogap state of the high-$T_c$ superconductor $Bi_2Sr_2CaCu_2O_{8+\delta}$. *Science* **303,** 1995–1998 (2004).
4. McElroy, K. *et al.* Destruction of antinodal state coherence via 'checkerboard' charge ordering in strongly underdoped superconducting $Bi_2Sr_2CaCu_2O_{8+\delta}$. Preprint at ⟨http://arXiv.org/cond-mat/0406491⟩ (2004).
5. Howald, C., Fournier, P. & Kapitulnik, A. Inherent inhomogeneities in tunneling spectra of $Bi_2Sr_2CaCu_2O_{8-x}$ crystals in the superconducting state. *Phys. Rev. B* **64,** 100504 (2001).
6. Cren, T., Roditchev, D., Sacks, W. & Klein, J. Nanometer scale mapping of the density of states in an inhomogeneous superconductor. *Europhys. Lett.* **54,** 84–90 (2001).
7. McElroy, K. *et al.* Relating atomic-scale electronic phenomena to wave-like quasiparticle states in superconducting $Bi_2Sr_2CaCu_2O_{8+\delta}$. *Nature* **422,** 592–596 (2003).
8. Ronning, F. *et al.* Photoemission evidence for a remnant Fermi surface and a *d*-wave-like dispersion in insulating $Ca_2CuO_2Cl_2$. *Science* **282,** 2067–2072 (1998).
9. Ronning, F. *et al.* Evolution of a metal to insulator transition in $Ca_{2-x}Na_xCuO_2Cl_2$ as seen by angle-resolved photoemission. *Phys. Rev. B* **67,** 165101 (2003).
10. Hiroi, Z., Kobayashi, N. & Takano, M. Probable hole-doped superconductivity without apical oxygens in $(Ca, Na)_2CuO_2Cl_2$. *Nature* **371,** 139–141 (1994).
11. Kohsaka, Y. *et al.* Growth of Na-doped $Ca_2CuO_2Cl_2$ single crystals under high pressures of several GPa. *J. Am. Chem. Soc.* **124,** 12275–12278 (2002).
12. Kohsaka, Y. *et al.* Imaging nano-scale electronic inhomogeneity in lightly doped Mott insulator $Ca_{2-x}Na_xCuO_2Cl_2$. *Phys. Rev. Lett.* (2004) (in the press); preprint at ⟨http://arXiv.org/cond-mat/0406089⟩.
13. Wei, J. Y. T. *et al.* Quasiparticle tunneling spectra of the high-$T_c$ mercury cuprates: Implications of the *d*-wave two-dimensional van Hove scenario. *Phys. Rev. B* **57,** 3650–3662 (1998).
14. Fu, H. C., Davis, J. C. & Lee, D.-H. On the charge ordering observed by recent STM experiments. Preprint at ⟨http://arXiv.org/cond-mat/0403001⟩ (2004)
15. Varma, C. M. Non-Fermi-liquid states and pairing instability of a general model of copper oxide metals. *Phys. Rev. B* **55,** 14554–14580 (1997).
16. Chakravarty, S., Laughlin, R. B., Morr, D. K. & Nayak, C. Hidden order in the cuprates. *Phys. Rev. B* **63,** 094503 (2001).
17. Lee, P. A. Pseudogap and competing states in underdoped cuprates. Preprint at ⟨http://arXiv.org/cond-mat/0307508⟩ (2003).
18. Zaanen, J. & Gunnarsson, O. Charged magnetic domain lines and the magnetism of high-$T_c$ oxides. *Phys. Rev. B* **40,** 7391–7394 (1989).
19. Machida, K. Magnetism in $La_2CuO_4$ based compounds. *Physica C* **158,** 192–196 (1989).
20. White, S. R. & Scalapino, D. J. Phase separation and stripe formation in the two-dimensional *t-J* model: A comparison of numerical results. *Phys. Rev. B* **61,** 6320–6326 (2000).
21. Emery, V. J., Kivelson, S. A. & Tranquada, J. M. Stripe phases in high-temperature superconductors. *Proc. Natl Acad. Sci. USA* **96,** 8814–8817 (1999).
22. Sachdev, S. Quantum criticality: Competing ground states in low dimensions. *Science* **288,** 475–480 (2000).
23. Bosch, M., van Saarloos, W. & Zaanen, J. Shifting Bragg peaks of cuprate stripes as possible indications for fractionally charged kinks. *Phys. Rev. B* **63,** 092501 (2001).
24. Kivelson, S. A., Fradkin, E. & Emery, V. J. Electronic liquid-crystal phases of a doped Mott insulator. *Nature* **393,** 550–553 (1998).
25. Vojta, M. Superconducting charge-ordered states in cuprates. *Phys. Rev. B* **66,** 104505 (2002).
26. Podolsky, D., Demler, E., Damle, K. & Halperin, B. I. Translational symmetry breaking in the superconducting state of the cuprates: Analysis of the quasiparticle density of states. *Phys. Rev. B* **67,** 094514 (2003).
27. Chen, H.-D., Vafek, O., Yazdani, A. & Zhang, S.-C. Pair density wave in the pseudogap state of high temperature superconductors. Preprint at ⟨http://arXiv.org/cond-mat/0402323⟩ (2004).
28. Chen, H.-D., Hu, J.-P., Capponi, S., Arrigoni, E. & Zhang, S.-C. Antiferromagnetism and hole pair checkerboard in the vortex state of high $T_c$ superconductors. *Phys. Rev. Lett.* **89,** 137004 (2002).
29. Tešanović, Z. Charge modulation, spin response, and dual Hofstadter butterfly in high-$T_c$ cuprates. Preprint at ⟨http://arXiv.org/cond-mat/0405235⟩ (2004).
30. Anderson, P. W. A suggested $4 \times 4$ structure in underdoped cuprate superconductors: a Wigner supersolid. Preprint at ⟨http://arXiv.org/cond-mat/0406038⟩ (2004).


**Supplementary Information** accompanies the paper on **www.nature.com/nature**.

**Acknowledgements** We acknowledge and thank P. Coleman, E. Demler, M. Franz, J. E. Hoffman, P. A. Lee, K. Machida, K. McElroy, D. Pines, S. Sachdev, T. Senthil, T. Timusk, M. Vojta and J. Zaanen for discussions and communications. This work was supported by the ONR, NSF, MEXT, JST and NEDO. C.L. acknowledges support from a NSERC Postdoctoral Fellowship and Y.K. from a JPSJ Research Fellowship for Young Scientists.

**Competing interests statement** The authors declare that they have no competing financial interests.

**Correspondence** and requests for materials should be addressed to J.C.D. (jcdavis@ccmr.cornell.edu) or T.H. (hanaguri@riken.jp).

# Detachment fronts and the onset of dynamic friction

**Shmuel M. Rubinstein, Gil Cohen & Jay Fineberg**

*The Racah Institute of Physics, The Hebrew University of Jerusalem, Givat Ram, Jerusalem, Israel*

**The dynamics of friction have been studied for hundreds of years, yet many aspects of these everyday processes are not understood. One such aspect is the onset of frictional motion (slip). First described more than 200 years ago as the transition from static to dynamic friction, the onset of slip is central to fields as diverse as physics[1–3], tribology[4,5], mechanics of earthquakes[6–11] and fracture[12–14]. Here we show that the onset of frictional slip is governed by three different types of coherent crack-like fronts: these are**

**observed by real-time visualization of the net contact area that forms the interface separating two blocks of like material. Two of these fronts, which propagate at subsonic and intersonic velocities, have been the subject of intensive recent interest[12–17]. We show that a third type of front, which propagates an order of magnitude more slowly, is the dominant mechanism for the rupture of the interface. No overall motion (sliding) of the blocks occurs until either of the slower two fronts traverses the entire interface.**

Consider the relative motion of two blocks of material which are separated by a rough interface. A force, $F_N$, is applied normal to the interface and a shear force, $F_S$, is applied in a direction parallel to the interface plane. We define 'slip' as differential motion along parts of the interface, while 'sliding' is defined as motion of the entire interface. More than 200 years ago, Coulomb and Amontons showed that the onset of motion occurs when $F_S = \mu_S F_N$, whereas continuous sliding is sustained for $F_S = \mu_D F_N$. The parameters $\mu_S$ and $\mu_D$ are, respectively, the static and dynamic coefficients of friction, where $\mu_S \geq \mu_D$. The modern study of dry friction (friction without lubrication) is rooted in the work of Bowden and Tabor[4], who explained this empirical relation as resulting from an increase of the net area of contact along the interface with increasing $F_N$. If the two blocks are not atomically smooth, the interface is made up of myriad randomly distributed 'micro-contacts', whose total surface area is smaller than the nominal contact area (that is, the cross-sectional contact area of the blocks) by orders of magnitude. When a normal force is first applied, the enormous initial pressure at its tip deforms each micro-contact[4]. This deformation (which may be either elastic or plastic) increases its contact area, thereby reducing the resultant pressure. These ideas were subsequently generalized by 'rate and state variable constitutive laws'[3,10,11,16,18,19], where an empirical state variable is introduced to describe the time dependence of the frictional interface. These laws have been successful in predicting stability criteria of frictional sliding[16] under changing loading conditions and contact history. Both direct calculations[17] as well as Coulomb and rate and state type frictional laws[7,9,20] have been used of late to model rapid motion within an interface formed by dissimilar materials. An interesting result of this work, in the context of earthquake dynamics[6,8,21], is the prediction of self-healing 'slip' pulses that propagate near the Rayleigh wave speed, $V_R$.

Our experiments study the dynamics of two brittle acrylic (polymethyl-methacrylate, PMMA) blocks separated by a rough interface, consisting of many discrete randomly distributed micro-contacts. Slip was initiated by increasing $F_S$ at a constant rate after setting a constant value of $F_N$. The experimental system (Fig. 1) was designed to allow light to pass through the interface only at the actual points of contact (see Methods for details). At all other points no light is transmitted, as the incident light undergoes total internal reflection at the interface. Thus, the light intensity, $I(x,y,t)$, passing through any region along the interface is proportional to the net local contact area $A(x,y,t)$. (Directions $x$ and $y$ are defined in Fig. 1a; $t$ is time.) Imaging of the transmitted intensity at sampling rates of up to 250,000 frames $s^{-1}$ enables us to visualize nearly instantaneous changes of $A(x,y,t)$. The linear dependence of the total intensity, $I$, on both $F_N$ (Fig. 2a) and the frictional force (Fig. 2b), $F_S = \mu_S F_N$ at the onset of slip, demonstrates the utility of the measurement system, and provides further[10] direct validation of the Bowden and Tabor picture of friction.

We use dynamic measurements of $I(x,y,t)$ to study the block detachment process (that is interface rupture) which gives rise to the onset of relative motion (sliding). These dynamics are governed by well-defined crack-like fronts (Fig. 3), which extend in the $y$ direction and propagate in the $x$ direction along the interface. We define these fronts as 'detachment fronts'. Behind a detachment front the net contact area is reduced, whereas ahead the contact area is unchanged. Three distinct types of detachment fronts, each with its own characteristic signature and velocity range, are observed.

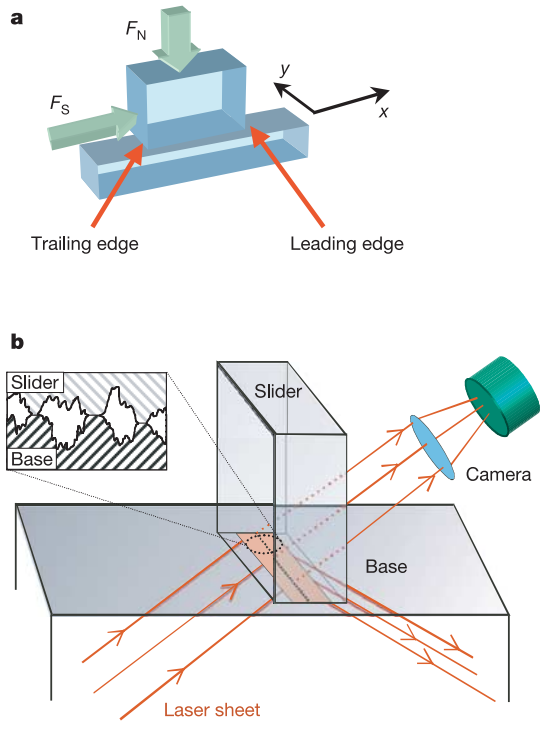


**Figure 1** A schematic diagram of the experimental apparatus. **a**, A normal force, $F_N$, is applied to the base and slider Plexiglas blocks. A shear force, $F_S$, applied at the trailing edge of the slider, is increased until motion ensues in the $x$ direction. **b**, A laser sheet, incident at an angle beyond the critical angle for total internal reflection, is solely transmitted at the net contact points along the rough interface (inset) between the base and slider. Thus, the light intensity transmitted across the interface at any location is proportional to the net contact area at that location. The transmitted light is imaged by a fast camera (see Methods for details).

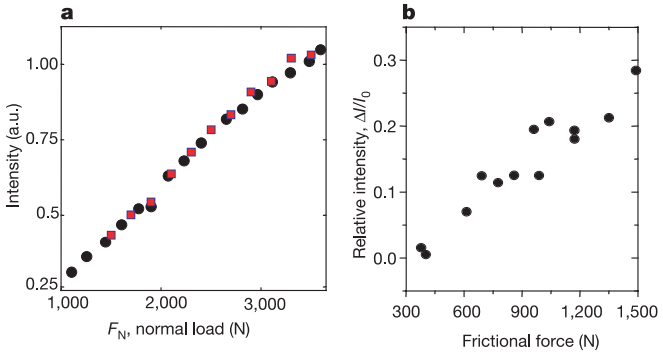


**Figure 2** The net contact area of the interface between two blocks of material is proportional to the applied force. **a**, Static measurements of the total intensity of light, $I$, transmitted across an interface as a function of the applied normal force, $F_N$. The linear dependence provides experimental verification of the proportionality of net contact area ($A$) with $F_N$, as predicted in ref. 4. The different symbols are taken from two different experiments. **b**, The critical shear force at the onset of frictional slip is proportional to transmitted intensity and hence to the net area $A$ across the interface. Shown are measurements from a number of different experiments of the change in transmitted intensity $\Delta I = (I - I_0)$ (immediately before slip), relative to the intensity $I_0$ of an initial load of $F_N = 750$ N. Each point is the average of four consecutive sliding events, separated in time by a 1 s interval. a.u., arbitrary units.

The detachment process is initiated by a single rapid 'sub-Rayleigh' front[15], which propagates along the interface at velocities that are always less than $V_R$. This subsonic front accelerates towards $V_R$ and bifurcates into two distinctly different types of detachment fronts; faint 'intersonic' fronts[12,13] that propagate at velocities that are beyond $V_R$, and slow detachment fronts that propagate along the interface at velocities over an order of magnitude slower than $V_R$.

This behaviour is demonstrated in Fig. 4. We measure the relative intensity integrated along the $y$ direction, $I(x,t)/I(x,0)$, which is equal to the relative change of the net local contact area as a function of time. Initially (at $t = 0$) there is no motion along the interface. Interface rupture is always initiated at the trailing edge of the sample, where the shear stress is applied ($x = 0$), owing to a small mechanical torque induced by the loading. A number of distinct propagating fronts are evident in the $(x,t)$ plot shown in Fig. 4a, whose velocity records are presented in Fig. 4b. The initial detachment at $x = 0$ is initiated by the sub-Rayleigh fronts, which then rapidly accelerate until they reach velocities in the vicinity of $V_R$ ($V_R = 930\,\mathrm{m\,s^{-1}}$ in PMMA). At approximately $V_R$ (see Fig. 4c), this subsonic front arrests and is replaced by both a slow detachment front and intersonic front[12–14,22], which are simultaneously emitted. Transitions from sub-Rayleigh to intersonic fronts[23] have been noted, but these studies were not able to observe the accompanying slow detachment fronts. The range of intersonic velocities that we measure are between 1,200 and 1,700 $\mathrm{m\,s^{-1}}$, with a $\pm 200\,\mathrm{m\,s^{-1}}$ accuracy. Note that shear cracks with point-like stress field singularities at their tip can propagate at all velocities up to a limiting velocity of $V_R$. Beyond $V_R$, only the special velocity of $\sqrt{2}V_S$, where $V_S$ is the shear wave velocity ($V_S = 1{,}000\,\mathrm{m\,s^{-1}}$ in PMMA), can support point-like singular modes[15]. Velocities between $\sqrt{2}V_S$ and the longitudinal wave speed are allowed if dissipation occurs in a region of finite size[13].

The velocities (between 40 and 80 $\mathrm{m\,s^{-1}}$) in Fig. 4b are typical for slow detachment fronts. As Fig. 4c demonstrates, these velocities are over an order of magnitude slower than those of other types of fronts, and 3–6 orders of magnitude faster than the driving velocity. In Fig. 4, the slow front does not reach the sample's leading edge, but undergoes a sharp reverse transition back to sub-Rayleigh fronts. Another example of this reverse transition occurs in Fig. 3 when a slow front (frames 2–5) jumps to sub-Rayleigh propagation (between frames 5 and 6). As seen in Fig. 5a, this reverse transition, though common, does not always occur.

An additional feature accompanying the onset of slip is the appearance of 'rebound' waves. Rebound waves, as indicated in Fig. 4a, are initiated at the leading edge of the sample upon the arrival of either sub-Rayleigh or slow detachment fronts. These waves propagate backwards across the interface at intersonic

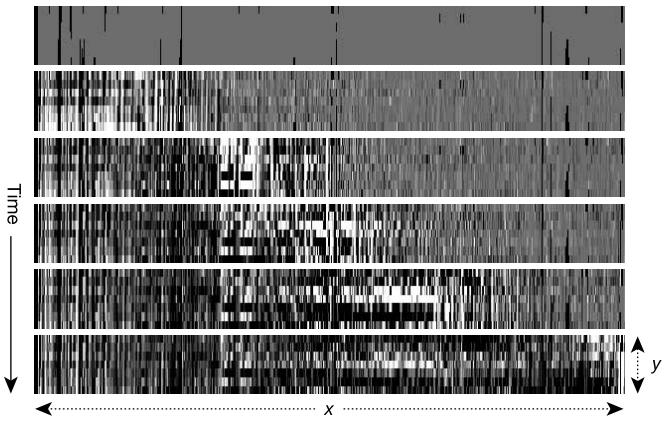


**Figure 3** The onset of slip occurs via coherent detachment fronts that propagate across the interface (from left to right). Behind these fronts the net contact area is reduced. Shown are six photographs of the net contact area of the interface between two blocks. The photographs are normalized by the net contact area at $t = 0$. The photographs, having spatial resolution of 1,280 × 16 pixels, were taken at (from top to bottom) times of 0, 0.4, 0.75, 1.00, 1.2 and 1.4 ms from the onset of the detachment process. The ($x \times y$) scales of each photograph are 140 × 6 mm. Dark (light) shades correspond to a decrease (increase) in contact area.

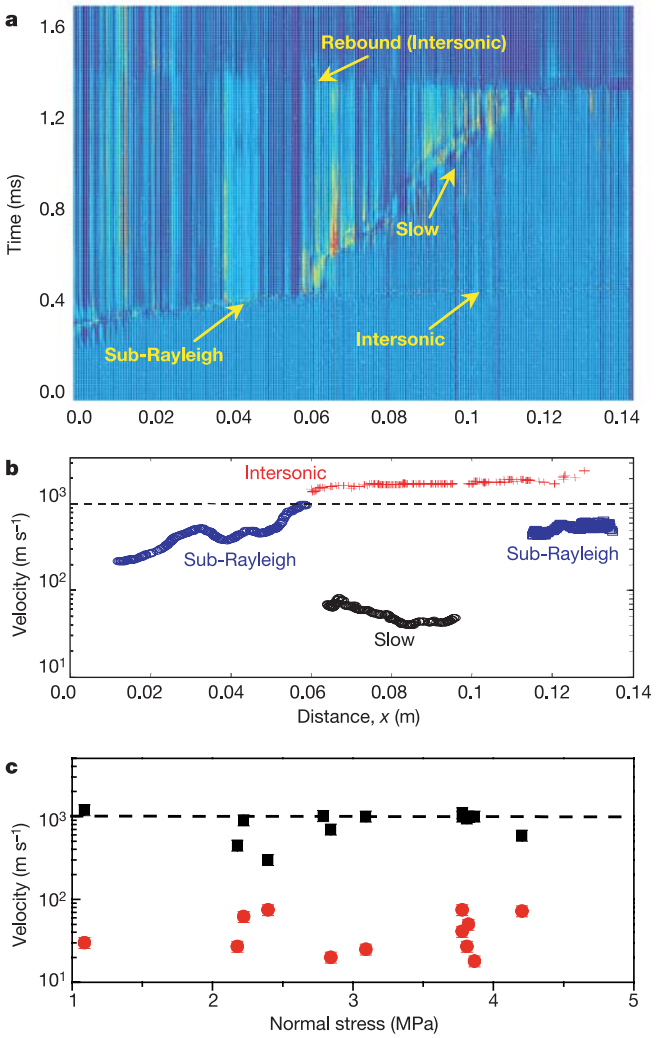


**Figure 4** The dynamics of slip, before overall sliding, take place via the interplay between four different types of coherent crack-like fronts. **a**, An $(x,t)$ plot of relative intensity measurements, averaged in the $y$ direction, of a typical experiment for $F_N = 3{,}470$ N, shear loading rate 40 $\mathrm{N\,s^{-1}}$ and driving velocity of 10 $\mu\mathrm{m\,s^{-1}}$ before the onset of slip and a 100,000 frames $\mathrm{s^{-1}}$ sampling rate. The intensity measurements, normalized by their initial values at each point, are colour-coded to reflect the change in the contact area at each spatial point as a function of time. Hot (cold) colours reflect increased (decreased) net contact area. The four different fronts (labelled within the graph) are clearly evident. **b**, Velocity records in space corresponding to the slow, sub-Rayleigh, and intersonic fronts seen in **a**. The rebound front (not shown in **b**) propagated in **a** at a mean velocity of 1,200 $\mathrm{m\,s^{-1}}$. **c**, The mean velocity values (rectangles) prior and (ovals) subsequent to the transition from sub-Rayleigh to slow fronts as a function of the applied normal stress in 13 different experiments. The velocities shown are mean values over spatial intervals (typically 1 cm) significantly larger than the front position uncertainty. Error bars represent the s.d. of each measurement. Note that the velocities of the two fronts differ by over an order of magnitude, and the mean velocity of the slow detachment fronts is six orders of magnitude more rapid than the rate (10 $\mu\mathrm{m\,s^{-1}}$) at which the shear stress is applied. In both **b** and **c** the dashed lines indicate $V_R$.

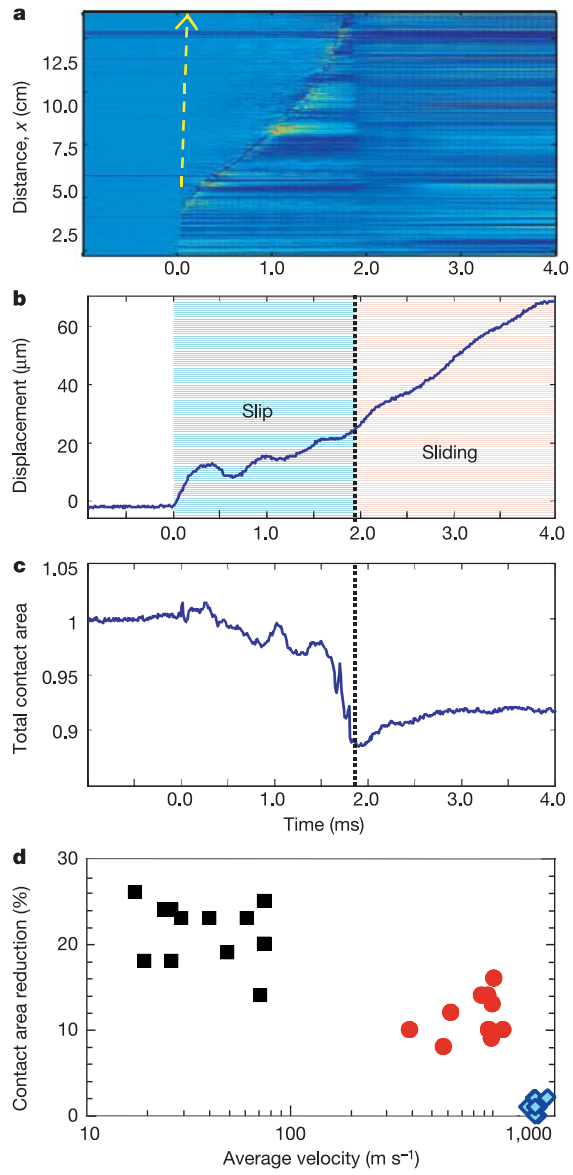


**Figure 5** Detailed dynamics of the detachment process. **a**, A $(t,x)$ plot of relative intensity measurements as a function of time for $F_N = 3{,}510$ N and a shear loading rate of 40 N s$^{-1}$ with a driving velocity of 10 μm s$^{-1}$ before the onset of slip. The intensity measurements are averaged in the $y$ direction. Colour coding is as in Fig. 4. The path of the intersonic pulse is highlighted by the dashed arrow. **b**, **c**, Corresponding records of the overall slip of the trailing edge of the sample (the edge where the shear force is applied) (**b**) and the integrated contact area along the entire interface (normalized by the initial contact area) (**c**) as a function of time. Dotted vertical lines in **b** and **c** indicate the arrival time of the slow front at the leading edge of the sample. The passage of the intersonic pulse results in both negligible (smaller than the estimated 10 μm intercontact distance) slip and a negligible reduction in contact area along the interface. Only about 30% of the total displacement of the trailing edge of the sample occurs before the arrival of the slow detachment pulse at the leading edge of the sample. At that time, the entire ~12% reduction of the contact area has occurred and only then is slip initiated at the leading edge. **d**, The mean reduction of contact area of the slow detachment fronts (rectangles), sub-Rayleigh fronts (ovals) and intersonic fronts (diamonds) as a function of their mean propagation velocities in 12 different experiments. The contact area reduction of the slow detachment fronts is, on average, twice that of the sub-Rayleigh fronts. The contact area reduction of the intersonic fronts is negligible. All measurements are sampled at 100 kHz. Note that the slight oscillations evident in **b** are due to the compliance of our displacement measurement apparatus (see Methods). This results in a displacement measurement error of 2.5 μm.

velocities of 1,300 ± 150 m s$^{-1}$. While forward-propagating intersonic fronts initiate erratic motion of the contact points along an interface, the process of self-organization of the interface is seen to subside immediately upon the passage of the rebound waves.

Simultaneous measurements of $I(x,t)/I(x,0)$ (Fig. 5a) and the slip of the trailing edge at $x = 0$ (Fig. 5b) show that significant slip of the trailing edge occurs as the contact area is reduced (Fig. 5c), although the majority of the trailing edge displacement occurs only after the detachment fronts have entirely traversed the sample. No displacement of the leading edge of the sample occurs until immediately following arrival of either slow or sub-Rayleigh fronts (dependent on whether a transition from a slow to a sub-Rayleigh front has occurred). Only then (dotted lines in Fig. 5b, c) does sliding ensue and the system passes from static to 'dynamic' friction. Negligible (smaller than the estimated intercontact distance of 10 μm) slip results from the passage of the intersonic fronts. The overall 12% reduction in the net contact area at the onset of sliding (Fig. 5c) signals the transition from static to dynamic friction. This is consistent with measured values (10–20%) of $(\mu_S - \mu_D)/\mu_S$ (ref. 3), although $\mu_D$ is well-defined only when steady-state sliding persists.

We now consider how efficiently each of the different fronts serves to reduce the net contact area along the interface. In Fig. 5d we present measurements of the relative intensity drop, $\Delta I/I(t = 0)$ (equivalent to a relative change, $\Delta A/A$, of the net contact area), that is precipitated by each type of detachment front. Surprisingly, the intersonic fronts give rise to negligible contact area reduction, with less than 2% of the contact area reduced by their passage. This may explain why these fronts lead to no overall slip. Although intersonic fronts certainly trigger interface fluctuations, they may only separate a small subpopulation of contact points, with the remaining contact points effectively anchoring the interface. Figure 5d further indicates that, in contrast, both the subsonic and slow detachment fronts effectively reduce the local contact area with their passage. The slow fronts are about twice as effective as their sub-Rayleigh counterparts, reducing the contact area by about 20%.

The dynamics of friction have, traditionally, been considered to be governed by processes that occur at slow timescales, when the entire slider is in motion. We have observed here the beginning of the transition to frictional sliding. A full description of these complex processes also involves[4] timescales much larger than those described here. Detachment fronts, such as those considered in this work, have been too rapid to be detectable in most studies of friction, although such fronts have been recently observed in studies of fault nucleation[24] and studies of gelatin sliding on glass[25]. These rapid processes are fundamental to fault nucleation and the onset of slip in earthquake dynamics. Sub-Rayleigh disturbances, propagating at velocities in the range of $(0.7–0.8)V_S$ for crustal (shallow) earthquakes and $(0.2–0.6)V_S$ in deep-focus earthquakes, have been inferred[26] from seismic records of a number of large earthquakes. Analysis of seismic data from the recent Izmit earthquake[27] suggests that a rupture front may have propagated at intersonic velocities, as observed in recent experiments[12,13]. Our measurements suggest that slow detachment fronts nearly always occur, either as isolated events or in conjunction with the more rapid modes. The slow fronts give rise to a significant amount of slip while in motion, but their acoustic signatures are significantly weaker than the faster modes. In an earthquake, these waves could therefore be masked, but could become apparent if a slip event were arrested before the transition to a rapid earthquake. Recent observations of slow or 'silent' earthquakes[28] in which significant slip was observed with a minimal acoustic signature[29,30] may, therefore, be analogous to these waves.

It is not yet clear if these fronts are related to self-healing pulses[6–9,11,17], which are predicted to propagate along bi-material interfaces, while generating spatially localized interface separation. Although contact area reduction is certainly observed, our measure-

ments show no indication of full interface separation at scales larger than a pixel. □

## Methods

The experiment was conducted using two PMMA (Plexiglas) blocks, a slider of size $150 \times 75 \times 6$ mm and a base of size $300 \times 270 \times 30$ mm in the $x$ (propagation), $y$ (sample thickness) and $z$ (normal loading) directions, respectively. The slider contact face was diamond-machined to a flatness of better than 0.1 μm (r.m.s.) and then roughened to 0.4–1 μm (r.m.s.). The base was also roughened to 1 μm (r.m.s.), thus defining the roughness of the interface to be approximately 1 μm.

Normal loading, $F_N$, was applied to the slider via a spring array (with a $4 \times 10^5$ N m$^{-1}$ stiffness), ensuring uniform stress distribution. The shear force, $F_S$, was applied by coupling a stepping motor to the slider via a load cell having a stiffness of $4 \times 10^6$ N m$^{-1}$. After the onset of slip, $F_S$ decreased by 5–8% as a result of this compliance, which is accompanied by a damped oscillation of the applied shear stress (having a maximum amplitude of about $0.005F_S$). The stepping motor moved in discrete steps of 0.04 μm with loading rates ranging from 1 μm s$^{-1}$ to 10 mm s$^{-1}$. Shear was applied to the sample 6.5 mm above the interface, thus introducing a small mechanical torque ($2.6 \times 10^{-3} F_N$ N m) in the loading. This resulted in a 2.5% variation of $F_N$ over the length of the interface. Applied normal and shear stresses ranged from 0 to 6 MPa and 0 to 3 MPa, respectively. Both applied forces and trailing edge displacement were measured by means of S-beam load cells. Measurement resolution of the displacement was 0.5 μm. This was further limited at the onset of slip by a resonant (2.5 μm) vibration of the system. Data acquisition was triggered by means of an acoustic sensor coupled to the leading edge of the slider.

The interface was illuminated by a $200 \times 5$ mm laser sheet through the base block at an angle significantly larger than the critical angle for total internal reflection from a PMMA/air interface. The (660 nm) laser light could transverse the slider–base interface either directly, at the micro-contact points between the two blocks, or by evanescence, where incident light (angle of incidence of 70°) tunnels across the air gap between the two blocks. The large ratio between the roughness (1 μm r.m.s.) of the interface and the exponential decay length (~50 nm) of the evanescent light enables us (over the range of normal forces applied) to neglect evanescent contributions to the intensity passing through the interface. Thus, the light passing through the interface is proportional to the area of net contact (see Fig. 2), where we consider 'net contact' as separation of less than 50 nm. A prism array was used to focus the transmitted light directly onto a fast CMOS sensor (VDS CMC1300 camera), enabling rapid imaging of the transmitted intensity. The sensor can be configured to frame sizes of $1{,}280 \times N$ pixels with frame rates of $500{,}000/(N+1)$ frames s$^{-1}$. In our experiments, the entire interface was measured; each pixel was mapped using cylindrical optics to either 117 μm × 1.5 mm ($\Delta x \times \Delta y$) at 100,000 frames s$^{-1}$ ($N = 4$) or 117 μm × 370 μm ($\Delta x \times \Delta y$) at 30,000 frames s$^{-1}$ ($N = 16$). These pixels encompass numerous contact points (we estimate the mean distance between contact points to be about 10 μm). All images presented were normalized pixel by pixel by the net contact area at time $t = 0$. In addition, to avoid noise-dominated weighting of the normalized data, pixels whose intensity in the reference image was lower than 1% of the maximal pixel intensity were excluded from all subsequent analyses.

Determination of the propagation velocities of the different fronts was performed as follows. The intensity measurements were first averaged in the $y$ direction to create a single array of intensities along the $x$ direction for each frame. Using these data, we obtained a time series of intensities measured at each spatial point (Figs 4a and 5a). To each time series one-dimensional wavelet transforms (Haar and db4 kernels) were applied to determine the arrival time of each of the different fronts at each spatial location along the interface (Fig. 4b). Differentiation of these data then yielded the velocity of each front.

Received 7 April; accepted 22 June 2004; doi:10.1038/nature02830.


1. Ciliberto, S. & Laroche, C. Energy dissipation in solid friction. *Eur. Phys. J. B* **9,** 551–558 (1999).
2. Muser, M. H., Wenning, L. & Robbins, M. O. Simple microscopic theory of Amontons's laws for static friction. *Phys. Rev. Lett.* **86,** 1295–1298 (2001).
3. Baumberger, T., Berthoud, P. & Caroli, C. Physical analysis of the state- and rate-dependent friction law. II. Dynamic friction. *Phys. Rev. B* **60,** 3928–3939 (1999).
4. Bowden, F. P. & Tabor, D. *The Friction and Lubrication of Solids* (Oxford Univ. Press, New York, 2001).
5. Persson, B. N. J. *Sliding Friction Physical Principles and Applications* (Springer, New York, 2000).
6. Heaton, T. H. Evidence for and implications of self-healing pulses of slip in earthquake rupture. *Phys. Earth Planet. Inter.* **64,** 1–20 (1990).
7. Cochard, A. & Rice, J. R. Fault rupture between dissimilar materials: Ill-posedness, regularization, and slip-pulse response. *J. Geophys. Res. B* **105,** 25891–25907 (2000).
8. Ben-Zion, Y. Dynamic ruptures in recent models of earthquake faults. *J. Mech. Phys. Solids* **49,** 2209–2244 (2001).
9. Andrews, D. J. & BenZion, Y. Wrinkle-like slip pulse on a fault between different materials. *J. Geophys. Res. B* **102,** 553–571 (1997).
10. Dieterich, J. H. & Kilgore, B. D. Direct observation of frictional contacts — new insights for state-dependent properties. *Pure Appl. Geophys.* **143,** 283–302 (1994).
11. Rice, J. R., Lapusta, N. & Ranjith, K. Rate and state dependent friction and the stability of sliding between elastically deformable solids. *J. Mech. Phys. Solids* **49,** 1865–1898 (2001).
12. Rosakis, A. J., Samudrala, O. & Coker, D. Cracks faster than the shear wave speed. *Science* **284,** 1337–1340 (1999).
13. Xia, K., Rosakis, A. J. & Kanamori, H. Laboratory earthquakes: The sub-Raleigh-to-supershear rupture transition. *Science* **303,** 1859–1861 (2004).
14. Gao, H. J., Huang, Y. G. & Abraham, F. F. Continuum and atomistic studies of intersonic crack propagation. *J. Mech. Phys. Solids* **49,** 2113–2132 (2001).
15. Freund, L. B. The mechanics of dynamic shear crack propagation. *J. Geophys. Res.* **84,** 2199–2209 (1979).
16. Scholz, C. H. Earthquakes and friction laws. *Nature* **391,** 37–42 (1998).
17. Gerde, E. & Marder, M. Friction and fracture. *Nature* **413,** 285–288 (2001).
18. Rice, J. R. & Ruina, A. L. Stability of steady frictional slipping. *J. Appl. Mech.* **50,** 343–349 (1983).
19. Kilgore, B. D., Blanpied, M. L. & Dieterich, J. H. Velocity dependent friction of granite over a wide range of conditions. *Geophys. Res. Lett.* **20,** 903–906 (1993).
20. Ben-Zion, Y. & Huang, Y. Q. Dynamic rupture on an interface between a compliant fault zone layer and a stiffer surrounding solid. *J. Geophys. Res. B* **107,** doi:10.1029/2001JB000254 (2002).
21. Anooshehpoor, A. & Brune, J. N. Wrinkle-like Weertman pulse at the interface between two blocks of foam rubber with different velocities. *Geophys. Res. Lett.* **26,** 2025–2028 (1999).
22. Bodin, P., Brown, S. & Matheson, D. Laboratory observations of fault-normal vibrations during stick slip. *J. Geophys. Res. B* **103,** 29931–29944 (1998).
23. Andrews, D. J. Rupture velocity of plane strain shear cracks. *J. Geophys. Res. B* **81,** 5679–5687 (1976).
24. Ohnaka, M. & Shen, L. F. Scaling of the shear rupture process from nucleation to dynamic propagation: Implications of geometric irregularity of the rupturing surfaces. *J. Geophys. Res. B* **104,** 817–844 (1999).
25. Baumberger, T., Caroli, C. & Ronsin, O. Self-healing slip pulses and the friction of gelatin gels. *Eur. Phys. J. E* **11,** 85–93 (2003).
26. Kanamori, H., Anderson, D. L. & Heaton, T. H. Frictional melting during the rupture of the 1994 Bolivian earthquake. *Science* **279,** 839–842 (1998).
27. Bouchon, M. *et al.* How fast is rupture during an earthquake? New insights from the 1999 Turkey earthquakes. *Geophys. Res. Lett.* **28,** 2723–2726 (2001).
28. Crescentini, L., Amoruso, A. & Scarpa, R. Constraints on slow earthquake dynamics from a swarm in central Italy. *Science* **286,** 2132–2134 (1999).
29. Linde, A. T. & Sacks, I. S. Slow earthquakes and great earthquakes along the Nankai trough. *Earth Planet. Sci. Lett.* **203,** 265–275 (2002).
30. Rogers, G. & Dragert, H. Episodic tremor and slip on the Cascadia subduction zone: The chatter of silent slip. *Science* **300,** 1942–1943 (2003).


**Acknowledgements** We thank Z. Reches, A. Sagy and M. Shay for comments. This research was supported by the Israel Science Foundation.

**Competing interests statement** The authors declare that they have no competing financial interests.

**Correspondence** and requests for materials should be addressed to J.F. (jay@vms.huji.ac.il).

# Ultrahigh-quality silicon carbide single crystals

**Daisuke Nakamura[1], Itaru Gunjishima[1], Satoshi Yamaguchi[1], Tadashi Ito[1], Atsuto Okamoto[1], Hiroyuki Kondo[2], Shoichi Onda[2] & Kazumasa Takatori[1]**

[1]*Toyota Central R&D Laboratories, Inc., Nagakute, Aichi, 480-1192, Japan*
[2]*Research Laboratories, DENSO Corporation, 500-1, Nissin, Aichi, 470-0111, Japan*

**Silicon carbide (SiC) has a range of useful physical, mechanical and electronic properties that make it a promising material for next-generation electronic devices[1,2]. Careful consideration of the thermal conditions[3–6] in which SiC {0001} is grown has resulted in improvements in crystal diameter and quality: the quantity of macroscopic defects such as hollow core dislocations (micropipes)[7–9], inclusions, small-angle boundaries and long-range lattice warp has been reduced[10,11]. But some macroscopic defects (about 1–10 cm$^{-2}$) and a large density of elementary dislocations (~$10^4$ cm$^{-2}$), such as edge, basal plane and screw dislocations, remain within the crystal, and have so far prevented the realization of high-efficiency, reliable electronic devices in SiC (refs 12–16). Here we report a method, inspired by the dislocation structure of SiC grown perpendicular to the *c*-axis (*a*-face growth)[17], to reduce the number of dislocations in SiC single crystals by two to three orders of magnitude, rendering them virtually dislocation-free. These substrates will promote the development of high-power SiC devices and reduce energy losses of the resulting electrical systems.**